

# Radiation Driven Surface Flows in Short-Period Massive-Star Binaries

R. H. D. Townsend<sup>1</sup>, N. R. Hill<sup>1</sup>, K. G. Gayley<sup>2</sup>, S. P. Owocki<sup>3</sup>

<sup>1</sup>*Department of Astronomy, University of Wisconsin-Madison, Madison, WI 53706, USA*

<sup>2</sup>*Department of Physics & Astronomy, University of Iowa, Iowa City, IA 52242, USA*

<sup>3</sup>*Bartol Research Institute, University of Delaware, Newark, DE 19716, USA*

Accepted Received

## ABSTRACT

Lorem ipsum dolor sit amet, consectetur adipiscing elit, sed do eiusmod tempor incididunt ut labore et dolore magna aliqua. Ut enim ad minim veniam, quis nostrud exercitation ullamco laboris nisi ut aliquip ex ea commodo consequat. Duis aute irure dolor in reprehenderit in voluptate velit esse cillum dolore eu fugiat nulla pariatur. Excepteur sint occaecat cupidatat non proident, sunt in culpa qui officia deserunt mollit anim id est laborum.

Lorem ipsum dolor sit amet, consectetur adipiscing elit, sed do eiusmod tempor incididunt ut labore et dolore magna aliqua. Ut enim ad minim veniam, quis nostrud exercitation ullamco laboris nisi ut aliquip ex ea commodo consequat. Duis aute irure dolor in reprehenderit in voluptate velit esse cillum dolore eu fugiat nulla pariatur. Excepteur sint occaecat cupidatat non proident, sunt in culpa qui officia deserunt mollit anim id est laborum.

## 1 INTRODUCTION

In short-period binary systems, the proximity of the stars means that effects arising from their mutual irradiation can become important. In low-mass binaries, the principal consequence is the so-called ‘reflection effect’, where an irradiated surface heats up to the point where it re-radiates the external radiation falling upon it (see, e.g., Wilson 1990, and references therein). The same effect will arise in massive-star binaries, but the immense radiative fluxes in these latter cases mean that radiative forces can also play a significant role.

Drechsel et al. (1995) argue that radiative forces can appreciably distort surface geometries in close massive-star binaries. They employ a formalism which represents these forces as the gradient of a scalar potential, allowing the surfaces of the components to be represented by a modified Roche potential. This formalism has proven quite popular in the literature (e.g., Phillips & Podsiadlowski 2002; Tsantilas et al. 2006; Palate et al. 2013).

In the present paper, we demonstrate that the Drechsel et al. (1995) formalism neglects re-emission of incident radiation. When taken into account, this re-emission results in the complete cancellation of the vertical component of the external radiative force; thus, no surface distortion is to be expected. However, the remaining horizontal component of the force can lead to surface flows, and we develop analytic (Section 2) and numerical (Section 3) treatments for these flows. In Section 4 we apply these treatments to model an O6V+O6V binary system, and explore the observational consequences of radiatively driven surface flows. Our findings are summarized in Section 5.

## 2 ANALYTIC TREATMENT

### 2.1 Radiation Field

We begin by considering the radiative acceleration of an atmosphere due to an external source of radiation. The following analysis draws extensively on the historical literature concerning the reflection effect, in particular the seminal studies by Eddington (1926) and Milne (1926). Given the approximations made in subsequent sections, it suffices to treat the irradiated atmosphere as both locally plane parallel and gray. Let  $I(\tau_z, \vartheta, \varphi)$  denote the frequency-integrated specific intensity of radiation at a vertical optical depth  $\tau_z$ , traveling in a direction given by the spherical polar colatitude  $\vartheta$  and azimuth  $\varphi$  (with the usual convention that the Cartesian  $z$  axis,  $\vartheta = 0$ , corresponds to the upward vertical direction). This specific intensity is conveniently expressed as the sum of three terms,

$$I(\tau_z, \mu, \varphi) = I_{\text{in}}(\tau_z, \vartheta) + I_{\text{ex}}(\tau_z, \vartheta, \varphi) + I_{\text{sc}}(\tau_z, \vartheta) \quad (1)$$

The  $I_{\text{in}}$  term represents the intrinsic radiation field of the unirradiated atmosphere, which carries away the luminosity generated in the stellar core. The external radiation is split into two parts: the  $I_{\text{ex}}$  term represents the external radiation that has yet to interact with the atmosphere (*‘... though attenuated [it] maintains its individuality at all depths’*; Milne 1926); while the  $I_{\text{sc}}$  term represents the radiation which has interacted one or more times with the atmosphere by scattering or thermalization; we assume that these processes are isotropic meaning that, like  $I_{\text{in}}$ ,  $I_{\text{sc}}$  is axisymmetric.

Without any loss of generality we assume the external radiation is a parallel beam with a flux  $F_{\text{ex}}$  per unit area normal to itself, traveling in the direction  $\vartheta = \vartheta_{\text{ex}} > \pi/2$

and  $\varphi = 0$ . Then,  $I_{\text{ex}}$  is given by the simple attenuation expression

$$I_{\text{ex}}(\tau_z, \vartheta, \varphi) = F_{\text{ex}} \delta(\vartheta_{\text{ex}} - \vartheta) \delta(\varphi) e^{-\tau_z / \cos \vartheta_{\text{ex}}}, \quad (2)$$

where  $\delta()$  is the Dirac delta function. Combining this with equation (1), and taking the first angular moments, yields expressions for the Cartesian components of the total flux vector  $\mathbf{F}$ :

$$F_x(\tau_z) = \sin \vartheta_{\text{ex}} F_{\text{ex}} e^{-\tau_z / \cos \vartheta_{\text{ex}}} \quad (3)$$

$$F_y(\tau_z) = 0 \quad (4)$$

$$F_z(\tau_z) = F_{\text{in}}(\tau_z) + \cos \vartheta_{\text{ex}} F_{\text{ex}} e^{-\tau_z / \cos \vartheta_{\text{ex}}} + F_{\text{sc}}(\tau_z), \quad (5)$$

where

$$F_{\text{in}}(\tau_z) = 2\pi \int_0^\pi I_{\text{in}}(\tau_z, \vartheta) \cos \vartheta d\vartheta \quad (6)$$

and similarly for  $F_{\text{sc}}$ .

At great depth ( $\tau_z \gg 1$ ) the atmosphere should remain unaffected by the external radiation, and thus  $F_z \rightarrow F_{\text{in}}$  there. Radiative equilibrium<sup>1</sup> requires that

$$\frac{dF_z}{d\tau_z} = 0, \quad (7)$$

and furthermore

$$\frac{dF_{\text{in}}}{d\tau_z} = 0; \quad (8)$$

hence, the identity  $F_z = F_{\text{in}}$  must hold at all depths, and not just for  $\tau_z \gg 1$ . This means that the vertical flux is *unaffected* by the external radiation, and as a corollary that

$$F_{\text{sc}}(\tau_z) = -\cos \vartheta_{\text{ex}} F_{\text{ex}} e^{-\tau_z / \cos \vartheta_{\text{ex}}}. \quad (9)$$

In the words of Eddington (1926), ‘*a star necessarily re-emits completely the radiation falling on it*’.

## 2.2 Radiative Acceleration

The foregoing analysis lays the groundwork for calculating the radiative acceleration  $\mathbf{g}_{\text{rad}}$ . For an isotropic opacity  $\kappa^2$ , this acceleration is

$$\mathbf{g}_{\text{rad}} = \frac{\kappa \mathbf{F}}{c}. \quad (10)$$

Combining this with equations (3–5), the non-vanishing Cartesian components of  $\mathbf{g}_{\text{rad}}$  are

$$g_{\text{rad},x}(\tau_z) = \frac{\kappa F_{\text{ex}}}{c} \sin \vartheta_{\text{ex}} e^{-\tau_z / \cos \vartheta_{\text{ex}}}, \quad (11)$$

$$g_{\text{rad},z}(\tau_z) = \frac{\kappa F_{\text{in}}}{c} + \frac{\kappa F_{\text{ex}}}{c} \cos \vartheta_{\text{ex}} e^{-\tau_z / \cos \vartheta_{\text{ex}}} + \frac{\kappa F_{\text{sc}}}{c}. \quad (12)$$

But by equation (9), the second and third terms in the expression for  $g_{\text{rad},z}$  must be equal and opposite; therefore,

$$g_{\text{rad},z}(\tau) = \frac{\kappa F_{\text{in}}}{c}, \quad (13)$$

<sup>1</sup> Since the present work focuses on hot, early-type stars, we can reasonably ignore any contributions toward thermal equilibrium by sub-surface convection.

<sup>2</sup> Anisotropic opacities typically result from the interaction between velocity gradients and line opacity sources, and can give rise to line-driven winds from irradiated stars (e.g., Gayley et al. 1999). The present analysis, however, is restricted to a consideration of *continuum* radiative driving.

and, like the flux, the vertical radiative acceleration in the atmosphere is unaffected by the external radiation.

In their treatment Drechsel et al. (1995) neglect the third term in equation (12), even though it is this term which exactly cancels the second. This casts serious doubt on their claim that significant modifications to stellar surface geometry might arise from irradiation by a binary companion. In fact, the consequences of such irradiation are to be found in the expression (11) for  $g_{\text{rad},x}$ . Since this component depends on  $\tau_z$ , it follows that  $\nabla \times \mathbf{g}_{\text{rad}} \neq 0$ . This in turn implies that it is impossible to balance the radiative force with any combination of gravitational, centrifugal or gas-pressure forces, all of which may be written as gradients of scalar functions. Thus, radiatively driven transverse flows are inevitable, just as a heavy wind must induce surface currents on a tranquil lake.

## 2.3 The Transverse Velocity

To constrain the surface flow pattern arising from the transverse radiative accelerations discussed above, we begin by considering the hydrodynamic momentum conservation equation, expressed in the frame of reference co-rotating with the star (e.g., Tassoul 2000),

$$\frac{\partial \mathbf{v}}{\partial t} + (\mathbf{v} \cdot \nabla) \mathbf{v} + 2\boldsymbol{\Omega} \times \mathbf{v} = -\frac{1}{\rho} \nabla p + \mathbf{g}_{\text{eff}} + \mathbf{g}_{\text{rad}} + \mathbf{g}_{\text{drag}} \quad (14)$$

Here,  $\mathbf{g}_{\text{eff}}$  is the effective gravitational acceleration, combining contributions from Newtonian gravity and the centrifugal force;  $\mathbf{g}_{\text{rad}}$  is the net radiative acceleration given by the expressions in the preceding section; and  $\mathbf{g}_{\text{drag}}$  is a generic drag term introduced for reasons we discuss below. For simplicity, it is assumed throughout that the rotation angular velocity vector  $\boldsymbol{\Omega}$  is constant, with magnitude  $\Omega$ , in both time and space.

Under the conditions of steady-state flow, the time derivative term in the above equation vanishes, leading to a vector condition

$$(\mathbf{v} \cdot \nabla) \mathbf{v} + 2\boldsymbol{\Omega} \times \mathbf{v} = -\frac{1}{\rho} \nabla p + \mathbf{g}_{\text{eff}} + \mathbf{g}_{\text{rad}} + \mathbf{g}_{\text{drag}} \quad (15)$$

prescribing force balance between the inertia and Coriolis terms on the left-hand side, and the effective gravity, pressure gradient, radiative and drag terms on the right-hand side. We do not explicitly concern ourselves with force balance in the vertical direction, since we assume that the atmospheric stratification remains largely unaffected by the external irradiation from the companion star, and by the surface flows established by this irradiation. This assumption is based largely on the observation that, as demonstrated in the preceding section, the external irradiation has no effect on the vertical component of  $\mathbf{g}_{\text{rad}}$ . Accordingly, the analysis now focuses exclusively on the transverse parts of equation (15).

It is evident from the  $\tau_z$  dependence of  $g_{\text{rad},x}$  (equation 11) that a different transverse flow equilibrium will be reached at each depth in the atmosphere, typically with the larger flow velocities at shallower depths where the radiative acceleration is stronger. Indeed, this follows naturally from the non-zero curl of the radiative force, discussed previously. Rather than attempting to simulate this complex shear flow, which would no doubt involve the treatment of

intricate phenomena such as Kelvin-Helmholtz instabilities and turbulence, we choose instead a simple model where the transverse velocity throughout the visible layers of the atmosphere is characterized by a single vector  $\bar{\mathbf{v}}(\theta, \phi)$  tangential to the stellar surface (here,  $\theta$  and  $\phi$  are now the polar and azimuthal angular coordinates in the global spherical polar coordinate system of the star). This vector is defined by averaging the flow velocity over the optical depth interval  $0 \leq \tau_z \leq 2/3$ ,

$$\bar{\mathbf{v}}(\theta, \phi) = \frac{3}{2} \int_0^{2/3} \mathbf{v}(\tau_z, \theta, \phi) d\tau_z. \quad (16)$$

If the opacity  $\kappa$  is assumed to be depth-independent, then  $\bar{\mathbf{v}}$  represents the mean momentum per unit mass throughout the visible layers.

A similar averaging can be applied to the transverse parts of equation (15), to obtain expressions for the components of  $\bar{\mathbf{v}}$ . In attempting to simplify these expressions, our initial efforts focused on achieving force balance solely between the transverse radiative acceleration and the flow inertia ( $\bar{\mathbf{v}} \cdot \nabla \bar{\mathbf{v}}$ ), with the assumption that the other terms would be unimportant. However, this resulted in highly supersonic velocities, that are neither observed nor physically plausible on the surface of stars, underlining the fact that for more-realistic subsonic flows, inertia is wholly insufficient at balancing radiative forces. In fact, for subsonic flows, it seems more reasonable to assume instead that flow inertia itself is negligible (we review this assumption below in Section 2.4). Furthermore, recognizing that acoustic waves will tend to smooth out any pressure fluctuations, the pressure gradient term in equation (15) can also be expected to be unimportant.

This then leaves the remaining Coriolis, radiative and drag forces to determine the transverse velocity. First considering the case of a spherical stellar surface (the generalization to arbitrary surface geometries is deferred until Section 2.5),  $\bar{\mathbf{v}}$  is conveniently represented in terms of its components ( $\bar{v}_\theta, \bar{v}_\phi$ ) in the  $(\theta, \phi)$  directions. For transverse force balance, with inertia and pressure forces neglected, these components must satisfy the equations

$$\begin{aligned} -2\Omega \cos \theta \bar{v}_\phi &= \bar{g}_{\text{rad}, \theta} + \bar{g}_{\text{drag}, \theta}, \\ 2\Omega \cos \theta \bar{v}_\theta &= \bar{g}_{\text{rad}, \phi} + \bar{g}_{\text{drag}, \phi}. \end{aligned} \quad (17)$$

The terms appearing on the right-hand sides are the appropriate vertical averages of the components of  $\mathbf{g}_{\text{rad}}$  and  $\mathbf{g}_{\text{drag}}$ . Assuming that  $\kappa$  is depth-independent, the results of the preceding section can be used to derive the averaged components of  $\mathbf{g}_{\text{rad}}$  as

$$\begin{aligned} \bar{g}_{\text{rad}, \theta} &= \frac{\kappa \mathcal{A}(\mu_{\text{ex}}) F_{\text{ex}, \theta}}{c}, \\ \bar{g}_{\text{rad}, \phi} &= \frac{\kappa \mathcal{A}(\mu_{\text{ex}}) F_{\text{ex}, \phi}}{c}. \end{aligned} \quad (18)$$

Here  $(F_{\text{ex}, r}, F_{\text{ex}, \theta}, F_{\text{ex}, \phi})$  are the  $(r, \theta, \phi)$  components of the external flux vector  $\mathbf{F}_{\text{ex}}$ , with

$$\mu_{\text{ex}} = -F_{\text{ex}, r} / |\mathbf{F}_{\text{ex}}|, \quad (19)$$

while the attenuation function  $\mathcal{A}(\mu_{\text{ex}})$  is introduced as

$$\mathcal{A}(\mu) = \frac{3}{2} \int_0^{2/3} e^{-\tau/\mu} d\tau = \frac{3}{2} \mu \left( 1 - e^{-2/3\mu} \right). \quad (20)$$

Strictly speaking, these expressions are only applicable when

the external radiation is a parallel beam; however, we assume for simplicity we can also apply them to a divergent beam.

To complete the derivation, we must consider the drag term  $\mathbf{g}_{\text{drag}}$ . This term is included to allow force balance around the stellar rotational equator, because there the Coriolis force has no transverse component. Physically, the drag term represents viscous coupling with the deeper, near-stationary parts of the star, that tends to decelerate the moving visible layers. The simplest treatment of the drag is to express it as a deceleration proportional to  $\bar{\mathbf{v}}$ ,

$$\mathbf{g}_{\text{drag}} = -\frac{\bar{\mathbf{v}}}{t_b}. \quad (21)$$

Here  $t_b$  is a characteristic braking timescale, a free parameter of our model.

Substituting equations (18) and (21) into the right-hand sides of (17), and solving the resulting linear system, the components of averaged flow velocity in the visible layers are found as

$$\begin{aligned} \bar{v}_\theta &= \frac{t_b \kappa \mathcal{A}(\mu_{\text{ex}})}{c(1 + \beta^2 \cos^2 \theta)} (F_{\text{ex}, \theta} + \beta \cos \theta F_{\text{ex}, \phi}), \\ \bar{v}_\phi &= \frac{t_b \kappa \mathcal{A}(\mu_{\text{ex}})}{c(1 + \beta^2 \cos^2 \theta)} (F_{\text{ex}, \phi} - \beta \cos \theta F_{\text{ex}, \theta}), \end{aligned} \quad (22)$$

where now the Coriolis parameter

$$\beta = 2\Omega t_b \quad (23)$$

quantifies how far the star rotates during a braking time, and characterizes whether Coriolis or drag effects will dominate the flow.

## 2.4 General properties of the flow

From the above equation (22) for the components of the averaged transverse velocity  $\bar{\mathbf{v}}$ , the flow speed at any point is derived as

$$|\bar{\mathbf{v}}| = \frac{t_b \kappa \mathcal{A}(\mu_{\text{ex}})}{c} \sqrt{\frac{F_{\text{ex}, \theta}^2 + F_{\text{ex}, \phi}^2}{1 + \beta^2 \cos^2 \theta}}. \quad (24)$$

This expression illustrates the necessity of including a drag term in the force balance condition; in the limit  $1/t_b \rightarrow 0$  of no drag, the flow speed would become infinite around the equator.

The flow direction, measured clockwise from the easterly direction, can likewise be found as

$$\tan \varpi \equiv \frac{\bar{v}_\theta}{\bar{v}_\phi} = \frac{F_{\text{ex}, \theta} + \beta \cos \theta F_{\text{ex}, \phi}}{F_{\text{ex}, \phi} - \beta \cos \theta F_{\text{ex}, \theta}}. \quad (25)$$

From this equation, we identify two regimes. In the drag-dominated limit  $|\beta \cos \theta| \ll 1$ , the flow direction is given by

$$\tan \varpi = \frac{F_{\text{ex}, \theta}}{F_{\text{ex}, \phi}}, \quad (26)$$

which is parallel to the transverse component of the external flux. Conversely, in the opposite Coriolis-dominated limit  $|\beta \cos \theta| \gg 1$ , the direction is

$$\tan \varpi = \begin{cases} \frac{F_{\text{ex}, \phi}}{-F_{\text{ex}, \theta}} & \mu > 0, \\ \frac{-F_{\text{ex}, \phi}}{F_{\text{ex}, \theta}} & \mu < 0, \end{cases} \quad (27)$$

which is now perpendicular to the transverse component of

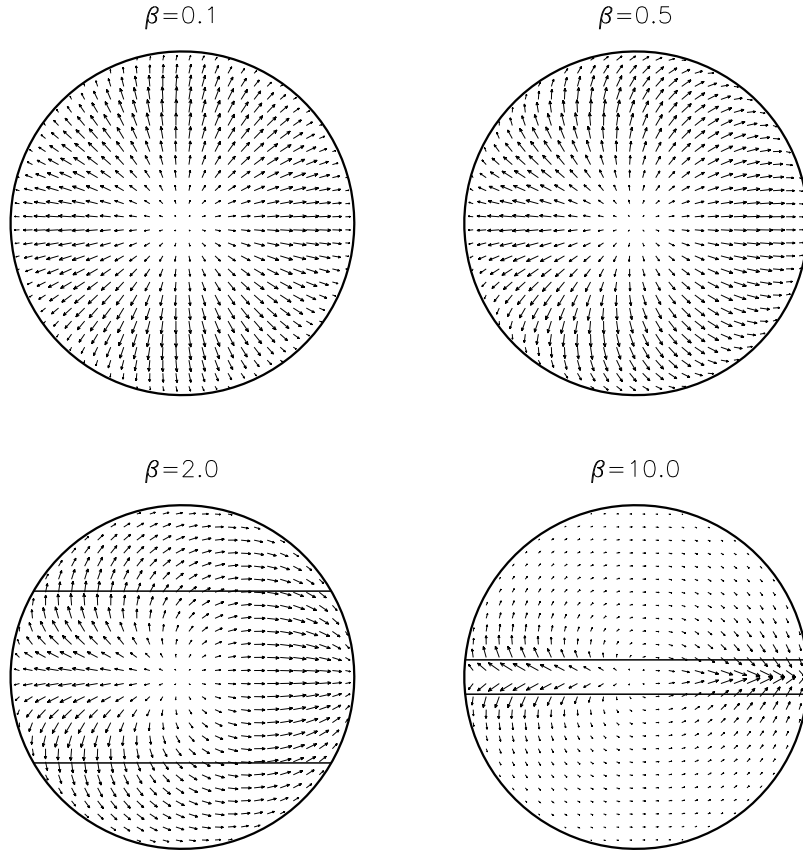


**Figure 1.** Flow patterns on the surface of a spherical star irradiated by a parallel beam, for four values of the Coriolis parameter  $\beta$ . The horizontal lines in the lower panels indicate the location of the critical boundaries  $\cos \theta = \pm 1/\beta$  that separate Coriolis- and drag-dominated flows.

the external flux. If  $\beta > 1$ , then a pair of critical boundaries  $\cos \theta = \pm 1/\beta$  can be defined on the stellar surface, that segregate the Coriolis-dominated perpendicular flows, in the polar regions, from the drag-dominated parallel flows around the equator.

To illustrate the foregoing discussion, we consider the simple case of a spherical star illuminated by a parallel beam coming from the  $(\theta, \phi) = (\pi/2, 0)$  direction. For such a configuration, the external flux has components

$$\begin{aligned} F_{\text{ex},r} &= -F_{\text{ex}} \sin \theta \cos \phi \\ F_{\text{ex},\theta} &= -F_{\text{ex}} \cos \theta \cos \phi \\ F_{\text{ex},\phi} &= F_{\text{ex}} \sin \phi \end{aligned} \quad (28)$$

and the components of the transverse velocity, over the irradiated hemisphere ( $|\phi| < \pi/2$ ) follow from equation (22) as

$$\begin{aligned} \bar{v}_\theta &= \frac{t_b \kappa \mathcal{A}(\mu_{\text{ex}}) F_{\text{ex}}}{c(1 + \beta^2 \cos^2 \theta)} (-\cos \theta \cos \phi + \beta \cos \theta \sin \phi), \\ \bar{v}_\phi &= \frac{t_b \kappa \mathcal{A}(\mu_{\text{ex}}) F_{\text{ex}}}{c(1 + \beta^2 \cos^2 \theta)} (\sin \phi + \beta \cos^2 \theta \cos \phi), \end{aligned} \quad (29)$$

where now

$$\mu_{\text{ex}} = \sin \theta \cos \phi. \quad (30)$$

Figure 1 shows the flow patterns predicted by these expressions, for four differing values of the parameter  $\beta$ . The

$\beta = 0.1$  and  $\beta = 10.0$  panels are particularly instructive, since they reveal the geometry in the drag- and Coriolis-dominated limits. In the former case, the flow is everywhere directed away from the center of the stellar disk, corresponding to the point where the radiative acceleration is normal to the surface. In the Coriolis-dominated case, however, the pattern is rather more complex. The speed is highest around the equator, due to the denominator in equation (24), and in each hemisphere takes the form of a large whorl that diverts initially-westward flowing material back around toward the easterly direction. In *both* cases, the flow speed becomes small at the stellar limb; this is because the external radiation is almost tangent to the surface there, and therefore barely penetrates into the atmosphere.

The flow patterns illustrated in Figure 1 indicate that  $\bar{\mathbf{v}}$  is strongly divergent in the transverse direction, and therefore — in the steady state — the flow would appear not to conserve mass. However, we anticipate that a system of return currents will quickly establish themselves beneath the visible layers. These currents, linked to the surface flows by an upwelling at the point where the radiative acceleration is normal to the surface (i.e., the disk center in the figure), and by downwellings at the terminator of the irradiated region, will ensure that mass is conserved globally.

To bring the present section to a close, we briefly re-

view the approximation that the inertia term  $\mathbf{i} \equiv (\bar{\mathbf{v}} \cdot \nabla)\bar{\mathbf{v}}$  can be neglected when determining the transverse flow velocity. This term scales as  $\sim |\bar{\mathbf{v}}|^2/R$ , with  $R$  the stellar radius, whereas the acceleration in the drag-dominated limit ( $\beta \lesssim 1$ ) scales as  $\sim |\bar{\mathbf{v}}|/t_b$  (cf. equation. 21). Thus, neglecting  $\mathbf{i}$  is reasonable when the braking length  $\ell_b \equiv t_b|\bar{\mathbf{v}}|$  is small compared with the stellar radius. With flow speeds being limited to the photospheric sound speed (for a hot star,  $a \sim 25 \text{ km s}^{-1}$ ), and anticipated breaking timescales extending up to  $\sim 10^4 \text{ s}$  (see Section 4.2), an upper limit on  $\ell_b$  is found as  $\sim 2.5 \times 10^8 \text{ m} \sim 0.36 R_\odot$ . This is much smaller than typical massive-star radii, and it follows that ignoring the inertia term in the present context should not lead to any serious errors. Indeed, for the flows plotted in Figure 1, we find in all cases that the magnitude of  $\mathbf{i}$  does not exceed 10% of the other terms appearing in the force-balance equation (15).

## 2.5 Formulation for non-spherical stars

In the foregoing analysis, we develop expressions for the flow velocity  $\bar{\mathbf{v}}$  under the assumption that the surface the star remains spherical. In a binary system, this is clearly not the case. However, it is straightforward to demonstrate that the transverse flow velocity can also be expressed as

$$\bar{\mathbf{v}} = \frac{t_b \kappa \mathcal{A}(\mu_{\text{ex}})}{c(1 + \mu_\Omega^2 \beta^2)} [(\mathbf{e}_n \times \mathbf{F}_{\text{ex}}) + \mu_\Omega \beta \mathbf{F}_{\text{ex}}] \times \mathbf{e}_n, \quad (31)$$

where  $\mathbf{e}_n$  is the local unit vector normal to the surface, and

$$\mu_{\text{ex}} = -\frac{\mathbf{F}_{\text{ex}} \cdot \mathbf{e}_n}{F_{\text{ex}}}, \quad \mu_\Omega = \frac{\boldsymbol{\Omega} \cdot \mathbf{e}_n}{\Omega}, \quad (32)$$

are the normalized projections of the external flux vector and rotation angular frequency vector onto this normal. This simple form for  $\bar{\mathbf{v}}$  is valid for *arbitrary* surface geometries, and its independence from any specific coordinate system makes it far more practical than component equations such as (22).

## 3 NUMERICAL MODEL

### 3.1 Overview

To predict the observable consequences of the transverse surface flows described in the preceding section, we use the GLADOS spectral modeling code (Hill & Townsend, in preparation). Triangle-based meshes representing the surfaces of the binary components are constructed, using an iterative procedure to solve for the irradiating fluxes. These meshes are rasterized using GLADOS's smooth shading option to create property images comprised of pixels storing property values derived from the sky-projected mesh. For each pixel, an observer-directed specific intensity is synthesized; summing over all pixels then yields a model spectrum for the system.

### 3.2 Mesh Generation

The mesh for each binary component is generated by applying the regularized marching tetrahedra (RMT) algorithm to the appropriate Roche potential  $\Phi_e$ , as described in section 3.2.3 of Hill & Townsend. The overall geometry of the system is set by specifying a mass  $M$  and polar radius  $R_p$

for each component, together with an orbital period  $P$ . We assume that the orbit is circular and the components rotate synchronously, since the focus here is on close systems.

The local surface normal vector  $\mathbf{e}_n$  and effective gravity  $g_{\text{eff}}$  at each mesh vertex are obtained directly from the gradient of the Roche potential,

$$\nabla \Phi_e = g_{\text{eff}} \mathbf{e}_n. \quad (33)$$

The effective temperature  $T_{\text{eff}}$  and transverse flow velocity  $\bar{\mathbf{v}}$  are calculated by first evaluating the external flux vector  $\mathbf{F}_{\text{ex}}$  on each triangular face. This involves an iterative procedure, similar to that outlined in Hendry & Mochnacki (1992, their section 3.2) but modified to handle vector fluxes. At each stage of the iteration, the flux vector for each face is updated via a discrete integral over the irradiating specific intensity,

$$\mathbf{F}_{\text{ex},i}^{k+1} = \sum_j I_j^k(\mu_{ij}) \mathbf{e}_{ij} \Delta \omega_{ij} \quad (34)$$

Here and throughout, the subscript  $i$  indexes the faces of one mesh, while  $j$  indexes the faces of the other, with the superscript  $k$  denoting the iteration stage. The unit vector  $\mathbf{e}_{ij}$  is defined as

$$\mathbf{e}_{ij} = \frac{\mathbf{r}_i - \mathbf{r}_j}{d_{ij}}, \quad (35)$$

where  $\mathbf{r}_i$  and  $\mathbf{r}_j$  are the position vectors of the face centers, and

$$d_{ij} = |\mathbf{r}_i - \mathbf{r}_j| \quad (36)$$

is their separation. The term  $I_j^k(\mu_{ij})$  denotes the  $k$ 'th-stage specific intensity, emergent from the  $j$ 'th face in a direction

$$\mu_{ij} = \mathbf{e}_{ij} \cdot \mathbf{e}_{n,j}, \quad (37)$$

relative to the local surface normal  $\mathbf{e}_{n,j}$ . Likewise, the  $\Delta \omega_{ij}$  term represents the solid angle subtended by the  $j$ 'th face at the  $i$ 'th face, which can be written in terms of the face area  $dA_j$  as

$$\Delta \omega_{ij} = \frac{\mu_{ij} dA_j}{d_{ij}^2}. \quad (38)$$

Note that the sum in equation (34) is taken only over those faces that can 'see' each other, such that  $\mathbf{e}_{ij} \cdot \mathbf{e}_{n,j} > 0$  and  $\mathbf{e}_{ij} \cdot \mathbf{e}_{n,i} < 0$ .

The specific intensity  $I_j^k(\mu)$  is calculated using the expression

$$I_j^k(\mu) = (F_{\text{in},j} - \mathbf{F}_{\text{ex},j}^k \cdot \mathbf{e}_{n,j}) \mathcal{R}(\mu). \quad (39)$$

Here,  $F_{\text{in},j}$  denotes the intrinsic outward flux of the  $j$ 'th face, calculated according to von Zeipel's 1924 gravity darkening law:

$$F_{\text{in},j} = \frac{g_{\text{eff},j} L}{\sum_{j'} dA_{j'} g_{\text{eff},j'}}, \quad (40)$$

where  $L$  is the intrinsic stellar luminosity (equal to the energy release rate in the core). The term  $\mathcal{R}(\mu)$  is what might be termed a 'specific intensity reconstruction function'; it converts an outgoing flux into a specific intensity that follows some prescribed limb-darkening law. Following (Hendry & Mochnacki 1992), we adopt a reconstruction function based on a quadratic limb-darkening law,

$$\mathcal{R}(\mu) = \frac{6 [1 - (1 - \mu)u_1 - (1 - \mu^2)u_2]}{\pi(6 - 2u_1 - 3u_2)}, \quad (41)$$

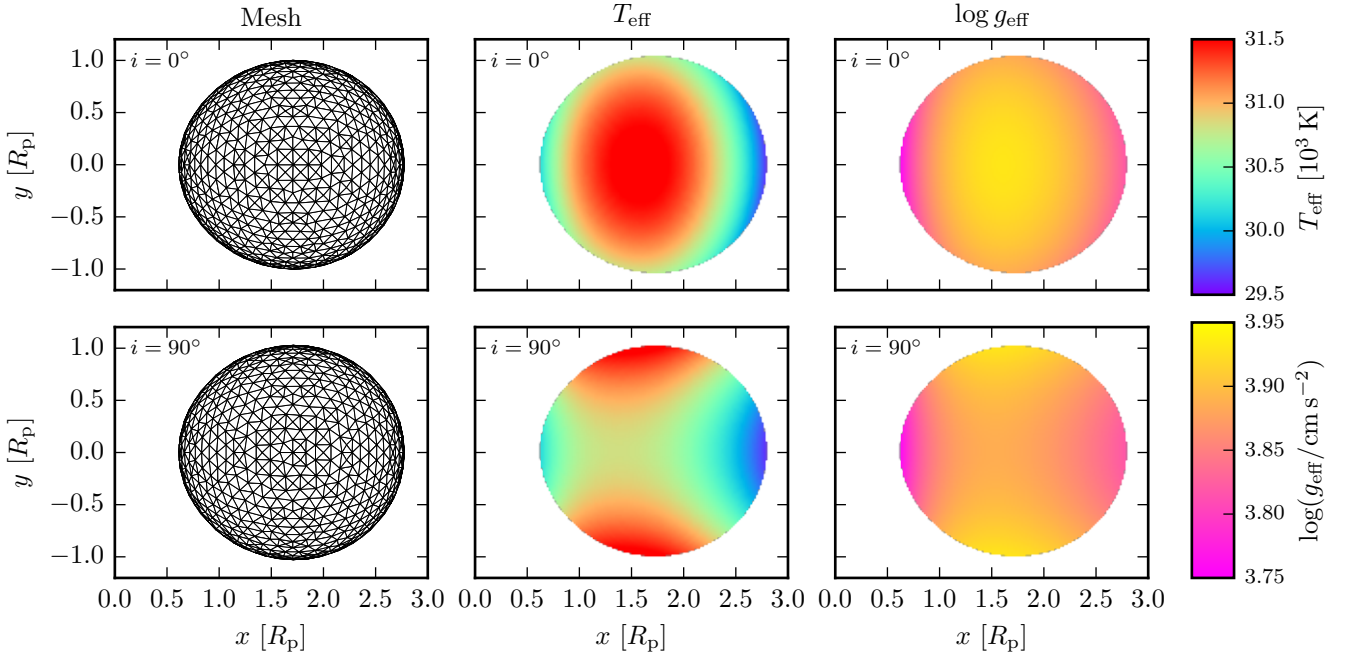


**Figure 2.** Mesh structure (left), effective temperature (center) and effective gravity (right) for the O6V+O6V model, plotted as a function of sky coordinates ( $x, y$ ) for pole-on (top) and equator-on (bottom) vantage.

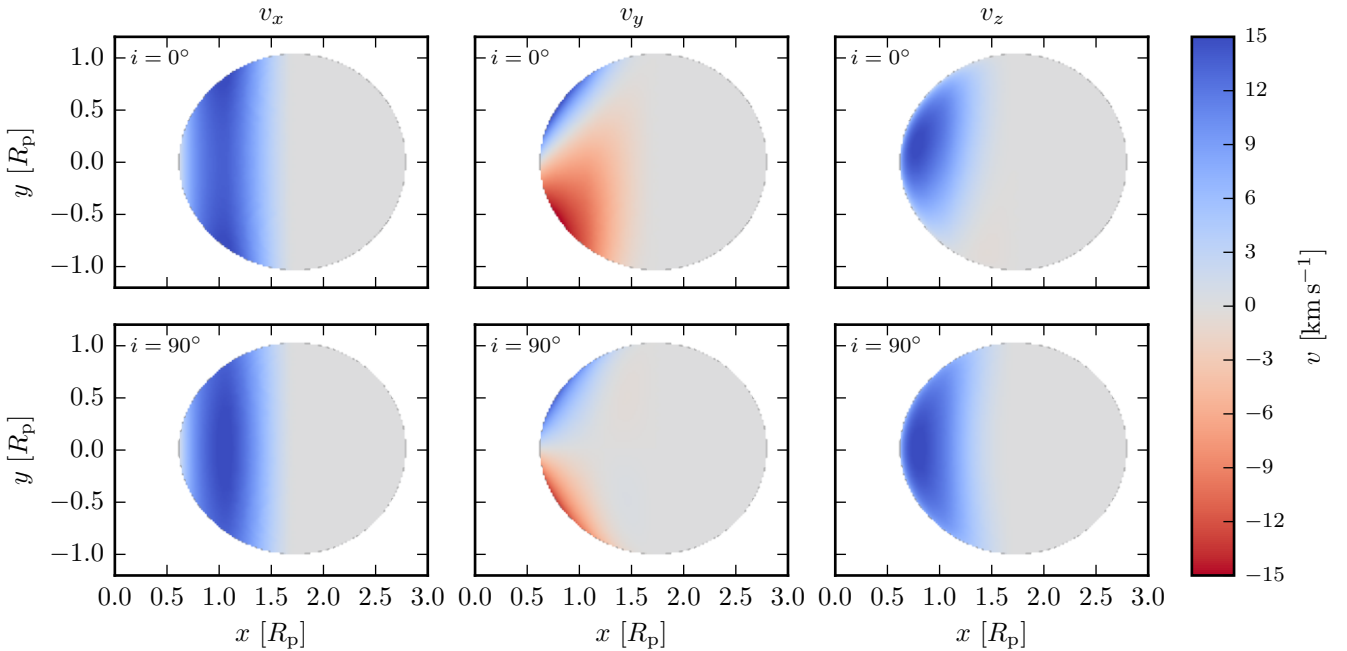


**Figure 3.** As in Figure 2, except that the Cartesian components of the velocity are now shown in the sky coordinate system (the  $z$  axis is directed out of the page).

with gray-atmosphere bolometric coefficients  $u_1 = 0.6500$  and  $u_2 = -0.0226$ . Note that equation (39) assumes the same reconstruction function for both intrinsic and reflected fluxes. This is not quite correct; as Milne (1926) first demonstrated, the reflected component is expected to show a limb darkening behavior that is rather different from intrinsic

component. Nevertheless, any error introduced by this simplification should be small.

The iterative procedure based on equation (34) converges quite rapidly to the external flux incident on each mesh face; for a fractional tolerance of  $10^{-3}$ , only  $\approx 4$  steps are required. Once converged, the corresponding flux vectors  $\mathbf{F}_{\text{ex}}$  on each vertex are calculated by averaging over

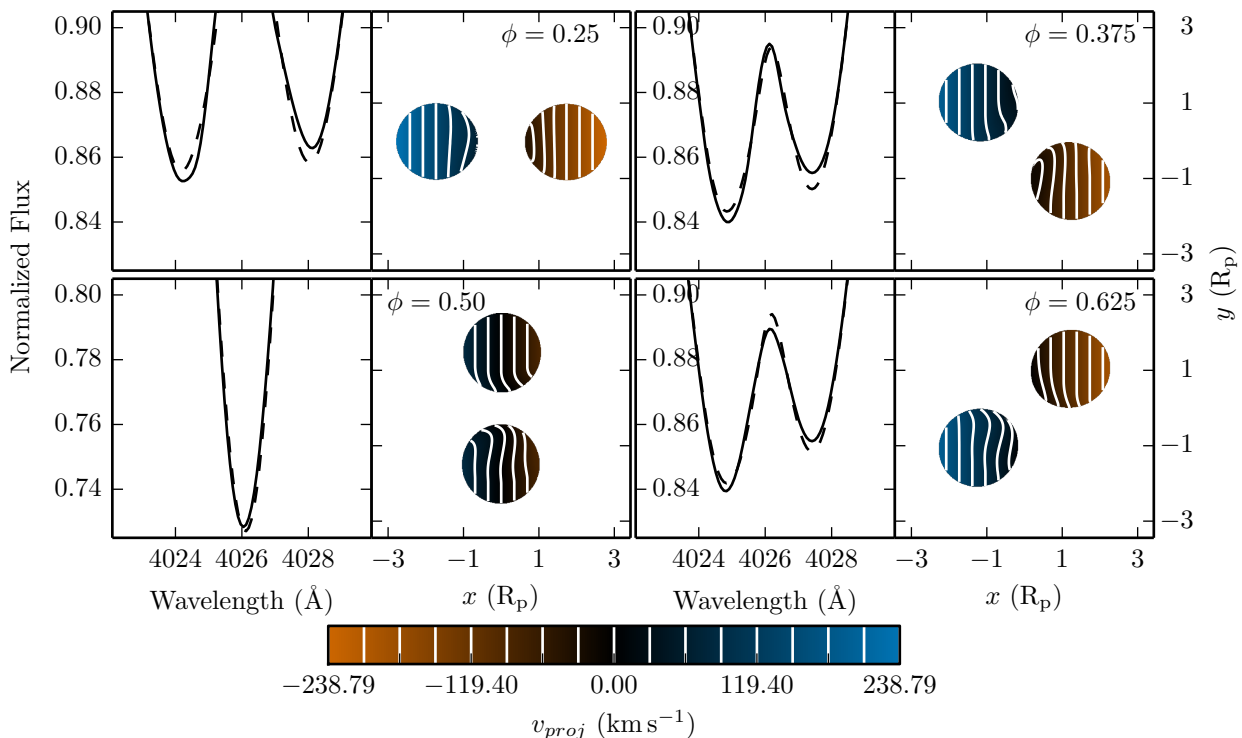


**Figure 4.** Snapshots of the isovelocity contours and He II 4026 Å line profiles for the O6+O6 model, at four selected orbital phases. Only the lower part of the line profiles is shown, in order to emphasize the depth differences. The dashed lines show the corresponding profiles in the absence of surface flows.

all faces that share that vertex. These vectors are used to obtain vertex values for the transverse flow velocity  $\bar{\mathbf{v}}$  via equation (31), and the local effective temperature  $T_{\text{eff}}$  via

$$\sigma T_{\text{eff}}^4 = F_{\text{in}} - \mathbf{F}_{\text{ex}} \cdot \mathbf{e}_n, \quad (42)$$

where the vertex intrinsic flux  $F_{\text{in}}$  is evaluated by similarly averaging over neighboring faces.

### 3.3 Spectral Synthesis

The per-pixel spectral synthesis step uses a grid of specific intensity spectra calculated with the SYNSPEC code (Lanz & Hubeny 2003) from solar-metallicity, non-LTE line-blanketed stellar atmosphere models: the OSTAR 2002 grid (Lanz & Hubeny 2003) for  $T_{\text{eff}} \geq 30,000$  K, and the BSTAR 2006 grid (Lanz & Hubeny 2007) for  $15,000 \text{ K} \leq T_{\text{eff}} \leq 30,000$  K. The adoption of these *unilluminated* atmospheres represents an approximation: equation (42) itself amounts to the assumption that the reflected radiation shares the same spectral distribution as the intrinsic radiation, and thus simply augments it. A more rigorous approach would involve self-consistent inclusion of the external irradiation in the atmosphere and specific intensity calculation (e.g., Vaz & Nordlund 1985), but this would introduce an enormous jump in the computational cost of simulations.

$M$ [ $M_{\odot}$ ]	$L$ [ $L_{\odot}$ ]	$R_p$ [ $R_{\odot}$ ]	$P$ (d)
31.73	88,300	10.23	3.0
$\kappa$ [ $\text{cm}^2 \text{g}^{-1}$ ]	$N_{\Delta}$	$dA_p$ [ $R_{\odot}^2$ ]	
1	64	$2.4 \times 10^{-5}$	

**Table 1.** Parameters for the O6V+O6V model.  $N_{\Delta}$  is the RMT resolution parameter, and  $dA_p$  the pixel area (see Hill & Townsend)

## 4 CALCULATIONS

### 4.1 Overview

We apply the numerical method described previously to explore the photometric and spectroscopic binary of a ‘matched’ massive-star binary system in which both components have  $M = 31.7 M_{\odot}$ . This mass corresponds to the O6V spectral type given in the calibration by Martins et al. (2005, their table 1), and the polar radius and luminosity of the stars are determined from the same calibration. Table 1 summarizes these and other parameters adopted for the modeling.

### 4.2 Surface Properties

Figure 2 illustrates the mesh structure and surface effective temperature and gravity of one star in the O6+O6 model, viewed at quadrature from pole-on ( $i = 0^\circ$ ) and equator-on ( $i = 90^\circ$ ) vantages. The center of mass of the system is at sky coordinates  $(x, y) = 0, 0$ , and the other star is the mirror image through  $x = 0$ .

The effective gravity is weakest around the equator, in

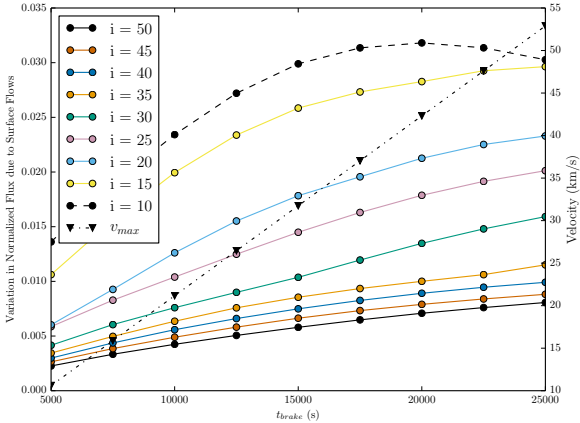


**Figure 5.** The difference (in continuum units) between the depths of the blue- and redshifted HeII 4026 Å line profiles for the O6+O6 model at quadrature, plotted as a function of braking timescale  $t_b$  for various choices of the inclination. The maximum surface flow velocity  $v_{\max}$  is also shown.

particular along the line of centers, due to partial cancellation between gravitational and centrifugal forces. The effective temperature follows the gravity due to equation (40), leading to hotter poles and cooler equatorial regions. However, the external radiation from the companion counteracts this gravity darkening on the inward-facing side of the star, raising the effective temperature at the substellar point  $(x, y) = (0.6, 0)$  by  $\approx 1,500$  K.

Figure 3 shows the Cartesian components of the surface flow velocity for the same model, calculated for a braking time  $t_b = 10^4$  sec. With  $\beta \approx 0.5$ , the flow follows the general behavior seen in the top-right panel of Figure 1: near the substellar point it is symmetric about the line of centers, but further away it is deflected eastward by the Coriolis force. The maximum flow velocity reached is  $\approx 15$  km s $^{-1}$ . We find empirically that this maximum varies approximately linearly with  $t_b$ , as would be predicted by equation (24) if we neglect the square-root term.

### 4.3 Line-Profile Variations

In the absence of surface flows, the isovelocity contours of a synchronous binary system appear as vertical lines parallel to the rotation axis. The principal consequence of the flows shown in Figure 3 is to deform these contours, making them wider apart on the star approaching the observer and narrower together on the star receding from the observer. Figure 4 illustrates this process in the O6+O6 model at four different orbital phases, for  $t_b = 10^4$  sec and an inclination  $i = 30^\circ$ . The  $\phi = 0.25$  (quadrature) panel in particular illustrates the contour widening (narrowing) on the approaching (receding) star.

The figure also plots profiles for the HeII 4026 Å line, calculated using GLADOS. When isovelocity contours are wider apart, the resulting profile is deeper than it would be in the absence of surface flows (shown in the figure by dashed lines); and vice-versa when the contours are narrower together. Thus, in spite of the fact that the stars are identical,

the line profiles at quadrature phase are always deeper for the approaching star, than for the receding star.

This behavior is strongly reminiscent of the so-called Struve-Sahade (SS) effect (see Howarth et al. 1997, and references therein), where the line profiles of the secondary component in a massive-star binary system are enhanced when blueshifted, relative to when redshifted. An example of the SS effect was reported by Arias et al. (2002) for HD 165052, an O6.5+O7.5 binary with a 2.955 d period. Their observed HeI 4471 Å line profile from the secondary appears to deepen by 10 – 20% when the secondary is approaching, compared to when it is receding. For comparison, the difference between the blue- and redshifted profiles in Figure 4 is  $\approx 0.015$  (in continuum units), corresponding to  $\approx 10\%$  of the overall profile depth. Therefore, it appears quite plausible that the SS effect is the observational consequence of the radiative surface flows we consider here.

To explore how the strength of the effect varies, Figure 6 plots the difference between the depths of the blue- and redshifted HeII 4026 Å profiles of the O6+O6 model, as a function of  $t_b$  for a variety of inclinations. The depth difference grows stronger as  $t_b$  increases, because the surface flows become progressively faster (the maximum velocity  $v_{\max}$  is also shown in the figure). It also is larger at lower inclinations, because — with a smaller projected rotation velocity — the isovelocity contours of the stars are more easily distorted by the surface flows.

## 5 SUMMARY

In the preceding sections we argue that external irradiation in a close massive star binary will not appreciably alter the shapes of the components, but instead will drive steady flows across their surfaces. We explore these flows using first an analytic model, and then a numerical model based on the GLADOS code. The principal observational signature of the flows is deeper line profiles when a star is approaching the observer, as compared to when the star is receding. This is the same behavior as seen in the Struve-Sahade effect, and thus our surface flows formalism seems a promising explanation for the effect. Further investigation is clearly required.

## ACKNOWLEDGMENTS

We acknowledge support from NSF Advanced Technology and Instrumentation grant AST-0904607. This research has made use of NASA’s Astrophysics Data System.

## REFERENCES

- Arias J. I., Morrell N. I., Barbá R. H., Bosch G. L., Grosso M., Corcoran M., 2002, MNRAS, 333, 202
- Drechsel H., Haas S., Lorenz R., Gayler S., 1995, A&A, 294, 723
- Eddington A. S., 1926, MNRAS, 86, 320
- Gayley K. G., Owocki S. P., Cranmer S. R., 1999, ApJ, 513, 442
- Hendry P. D., Mochnacki S. W., 1992, ApJ, 388, 603
- Howarth I. D., Siebert K. W., Hussain G. A. J., Prinja R. K., 1997, MNRAS, 284, 265



- Lanz T., Hubeny I., 2003, ApJS, 146, 417  
Lanz T., Hubeny I., 2007, ApJS, 169, 83  
Martins F., Schaerer D., Hillier D. J., 2005, A&A, 436, 1049  
Milne E. A., 1926, MNRAS, 87, 43  
Palate M., Rauw G., Koenigsberger G., Moreno E., 2013, A&A, 552, A39  
Phillips S. N., Podsiadlowski P., 2002, MNRAS, 337, 431  
Tassoul J.-L., 2000, Stellar Rotation. Cambridge University Press, New York  
Tsantilas S., Rovithis-Livaniou H., Djurasevic G., 2006, Ap&SS, 304, 117  
Vaz L. P. R., Nordlund A., 1985, A&A, 147, 281  
von Zeipel H., 1924, MNRAS, 84, 665  
Wilson R. E., 1990, ApJ, 356, 613